Final Report

EOARD Contract No F61775-00-WE012

Clear-air effects
on airborne sensors

M.F. Levy
Radio Communications Research Unit
Rutherford Appleton Laboratory
Chilton, Didcot, Oxon OX11 0QX
UK

http://www.rcru.rl.ac.uk

REPORT DOCUMENTATION PAGE

Form Approved OMB No. 0704-0188

Public reporting burden for this collection of information is estimated to average 1 hour per response, including the time for reviewing instructions, searching existing data sources, gathering and maintaining the data needed, and completing and reviewing the collection of information. Send comments regarding this burden estimate or any other aspect of this collection of information, including suggestions for reducing this burden to Washington Headquarters Services, Directorate for Information Operations and Reports, 1215 Jefferson Davis Highway, Suite 1204, Arlington, VA 22202-4302, and to the Office of Management and Budget, Paperwork Reduction Project (0704-0188), Washington, DC 20503.

1. AGENCY USE ONLY (Leave blank)	2. REPORT DATE 29-May-2001	3. REPORT TYPE AND DATES COVERED Final Report

4. TITLE AND SUBTITLE

Clear-Air Effects on Airborne Sensors

5. FUNDING NUMBERS

F61775-00-WE012

6. AUTHOR(S)

Dr. Mireille Florence Levy

7. PERFORMING ORGANIZATION NAME(S) AND ADDRESS(ES)

Council for the Central Laboratory of the Research Councils
Chilton
Didcot OX11 0QX
United Kingdom

8. PERFORMING ORGANIZATION REPORT NUMBER

N/A

9. SPONSORING/MONITORING AGENCY NAME(S) AND ADDRESS(ES)

EOARD
PSC 802 BOX 14
FPO 09499-0200

10. SPONSORING/MONITORING AGENCY REPORT NUMBER

SPC 00-4012

11. SUPPLEMENTARY NOTES

12a. DISTRIBUTION/AVAILABILITY STATEMENT

Approved for public release; distribution is unlimited.

12b. DISTRIBUTION CODE

A

13. ABSTRACT (Maximum 200 words)

This report results from a contract tasking Council for the Central Laboratory of the Research Councils as follows: The contractor shall investigate novel approaches to using stochastic modeling to study radar propogation in the UK AWACS. Simulated data will be used to study the impact of refractive index fluctuations due to turbulence and determine if these phenomena will fill the radar holes or deepen them. The deliverables will consist of a report describing the methodology and results and is due 6 months after contract award.

14. SUBJECT TERMS

EOARD, Radio Propagation, radar

15. NUMBER OF PAGES

31

16. PRICE CODE

N/A

17. SECURITY CLASSIFICATION OF REPORT UNCLASSIFIED	18. SECURITY CLASSIFICATION OF THIS PAGE UNCLASSIFIED	19. SECURITY CLASSIFICATION OF ABSTRACT UNCLASSIFIED	20. LIMITATION OF ABSTRACT UL

NSN 7540-01-280-5500

Standard Form 298 (Rev. 2-89)
Prescribed by ANSI Std. 239-18
298-102

Abstract

This report investigate the effects of atmospheric turbulence on the performance of airborne radars. The suitability of parabolic equation models for this application is investigated. We demonstrate that if the turbulent processes are assumed to be quasi-homogeneous and Gaussian, the most commonly used spectra lead to very weak refractive index gradients for individual realisations, even in strong turbulence, and that split-step parabolic equation models are adequate at the frequencies of interest.

Parabolic equation solutions for the moments of the field are derived in a particularly simple fashion which avoids the use of stochastic integrals, under the Markov approximation. Since the moment equations are more expensive computationally than Monte-Carlo simulations, which have the added advantage of not requiring the Markov approximation, we conclude that the Monte-Carlo option is the best one for this work. Monte-Carlo parabolic equation simulations involve the generation of random phase-screens to represent the integrated refractive index fluctuations over a range step. Correlation functions for the integrated fluctuations are given, both in the general case and under the Markov approximation.

The parabolic equation model available at the Radio Communications Research Unit includes advanced features like accurate treatment of the air/ground interface. This has been used to compute results for generic helicopter and AWACS examples, with both von Karman and Gaussian turbulence spectra. Results indicate that the turbulent layers may enhance or mitigate radar holes depending on the autocorrelation function of the refractive index. However these effects remain small even in strong turbulence unless we assume very strong range correlation. The most striking effects are obtained for frozen-in-range turbulence.

Contents

1 Introduction

Clear air effects such as ducting and turbulence greatly affect the performance of airborne radars [8]. Very little is known at present on the potential for mitigation of propagation effects by optimising platform stationing, for example when multiple AWACS are required to form an Air Defense Net. In particular it is not known whether atmospheric turbulence enhances or mitigates radar holes caused by atmospheric layering. Although some work has been carried out on this topic for ground-based sensors [8, 6], very little information is available so far on the airborne case, mainly because of the high computational burden associated with it. Here we use parabolic equation (PE) techniques [11] to model propagation in a stochastic medium, using phase-screen techniques along the lines of [22]. We note here that numerical phase-screen methods are widely used in atmospheric acoustics (see for example [2] and optics [20].

The parabolic equation framework can only be used if the propagation medium is smoothly varying on the scale of a wavelength. Hence it is crucial to check whether the irregularities caused by the random fluctuations of the atmospheric refractive index can violate smoothness constraints. We first give general results on stochastic processes in section 2. These are then applied to atmospheric refractive index fluctuations in section 3.

In section 4, we look at the PE solution for a single realisation of the field. This requires the generation of appropriate phase-screens representing the refractive index fluctuations integrated over a range step, a topic which is addressed in section 5. The solution for a single realisation is the building block for Monte-Carlo simulations, which can be used to compute the statistics of the field. Alternatively, it is possible to derive equations for the moments of the field under the Markov approximation. As this option provides results in closed form for propagation in a homogeneous medium, it has been favoured by many authors. We give a particularly simple derivation of the moment equations based on the split-step formulation of the PE solution in section 6.

In section 7, we look at turbulence effects on airborne antennas. We have selected a case study involving a 10 GHz source located at an altitude of 1500 m, corresponding to a generic helicopter radar, and a case study involving a 3 GHz source located at an altitude of 9000 m, corresponding to a generic AWACS radar. Finally section 8 gives conclusions and ideas for future work.

2 Regularity of Gaussian processes

If a given realisation of the random medium is sufficiently smooth, it will be possible to treat the problem for that particular realisation as propagation in a smoothly varying medium and to describe it in terms of the Maxwell equations. For general random processes there is no garantee at all that individual realisations (or sample paths) will be smooth. For example the sample paths of Brownian motion are continuous and nowhere differentiable,

1

with probability one [3]. Fortunately, for special classes of random processes, smooth paths are guaranteed by the existence of a sufficiently regular covariance function. We use terminology and results from the book by Cramér and Leadbetter [3], which gives a wealth of information on the regularity of sample paths.

We shall need a few definitions concerning random processes. In this section we consider real processes only.

A random process $X(\mathbf{r}, \omega)$ is **strictly homogeneous** if all joint distributions of variables of the form $(X(\mathbf{r}_1 + \mathbf{r}), \ldots, X_N(r_N + \mathbf{r})$ are independent of $\mathbf{r}$.

A random process $X(\mathbf{r}, \omega)$ is **Gaussian** if all joint distributions of variables of the form $(X(\mathbf{r}_1), \ldots, X_N(r_N$ are Gaussian.

If X is a real centred Gaussian process, then X is strictly stationary if and only if its covariance (or correlation) function) B defined by

$$B(\mathbf{r}) = \langle X(\mathbf{r}_1) X(\mathbf{r}_1 + \mathbf{r}) \rangle \tag{1}$$

does not depend of $\mathbf{r}_1$, where the angle brackets denote expectation in the probability space. Then X is entirely defined by its covariance function.

Frow now on we assume the covariance function is continuous. Then X has a spectral representation of the form

$$X(\mathbf{r}, \omega) = \int_{\mathbb{R}^3} e^{i\mathbf{K} \cdot \mathbf{r}} \sqrt{\Phi(\mathbf{K})} dW(\mathbf{K}, \omega) \tag{2}$$

where the stochastic integral is defined as a Fourier-Stiljes integral, W is a Wiener process and the power spectral density Φ is defined by

$$\Phi(\mathbf{K}) = \frac{1}{(2\pi)^3} \int_{\mathbb{R}^3} B(\mathbf{r}) e^{-i\mathbf{K} \cdot \mathbf{r}} d\mathbf{r} \tag{3}$$

This is the Wiener-Khintchine theorem [3, 9].

The following theorem, which follows from results in [3] summarises some sufficient conditions for sample paths to be well-behaved with probability one.

Theorem 1 *If the covariance function has second order partial derivatives at zero, then with probability one the sample paths have continuous partial derivatives. More generally if for some positive integer p the covariance function has partial derivatives up to order $2p$*

2

at zero, then the sample paths are continuously differentuable up to order p with probability one.

Since the covariance function is the inverse Fourier transform of the spectral density, conditions for regularity of the sample paths can also be written in terms of the spectral density: for example the covariance function is twice-differentiable if and only if the spectral density satisfies

$$\int_{\mathbb{R}^3} |\mathbf{K}|^2 \Phi(\mathbf{K}) d\mathbf{K} < \infty \tag{4}$$

As a result, we have the following theorem giving sufficient conditions on the spectrum for the sample paths to be regular with probability one.

Theorem 2 *If for some positive integer p the spectral density satisfies*

$$\int_{\mathbb{R}^3} |\mathbf{K}|^{2p} \Phi(\mathbf{K}) d\mathbf{K} < \infty \tag{5}$$

then the sample paths are continuously differentiable up to order p.

If follows that if the spectrum is well-behaved, the sample paths are very regular with probability one. This is already rather good news: provided the spectrum has good integrability properties, individual realisations of the refractive index fluctuations will be regular with probability one, which means we can treat each realisation of the random propagation medium as a smoothly varying medium.

Now in order to apply the parabolic approximation to Maxwell's equations, we shall need bounds on the refractive index slopes. It turns out that bounds can be obtained in terms of the spectrum [3]. Assume that the process X has continuous sample paths in the spatial domain D given by $0 \leq x \leq a, 0 \leq y \leq b, 0 \leq z \leq c$. Then for a given threshold u, we look at the random variable

$$V_u = \frac{1}{abc} \int_D 1_{|X(\mathbf{r})|>u} d\mathbf{r} \tag{6}$$

which is the proportional volume of the domain where $|X|$ exceeds u. Then the expectation of V_u is given by

$$\langle V_u \rangle = \text{erfc} \left(\frac{u}{\sqrt{2B(0,0,0)}} \right) \tag{7}$$

where the complementary error function erfc is defined by

3

$$\mathrm{erfc}(s) = \frac{2}{\sqrt{\pi}} \int_s^\infty e^{-t^2} dt \qquad (8)$$

It follows from equation 7 that if the variance of the process is small, $|X|$ will remain small in a large proportion of the domain. We can apply equation 7 to the derivatives of a random process to obtain estimates on the gradients of the sample paths. In the next section we carry this out for the most commonly used refractive index spectra in order to see whether the parabolic approximation is applicable.

3 Stochastic properties of the refractive index

We assume here that the propagation phenomena of interest happen in a very short time compared to the temporal fluctuations scales of the medium, and we treat the medium as frozen in time. For a more detailed analysis of the radar echoes produced by a moving target at a moving platform, it would certainly be necessary to include time fluctuations in the modelling.

For a spatial point $\mathbf{r} = (x, y, z)$ and a point ω in the probability space, we write the atmospheric refractive index $n(\mathbf{r}, \omega)$ as

$$n(\mathbf{r}, \omega) = 1 + n_d(\mathbf{r}) + n_f(\mathbf{r}, \omega) \qquad (9)$$

where n_f is a centred random variable representing the fluctuations of the refractive index. The quantity n_d represents the deterministic spatial variations of the medium.

In all that follows, we assume that the refractive index can be modelled as a Gaussian random process. This assumption may not always be realistic [16], but there is currently no real alternative in the absence of sufficiently resolved computational fluid dynamics models. Hybrid models extending large eddy simulations to subgrid scales have recently been introduced [6, 21], but computational requirements are still prohibitive for the very large domains required for our application.

We first look at the von Karman approximation of the Kolmogorov spectrum, which describes isotropic locally homogeneous turbulence in the inertial subrange, before moving to Gaussian spectra, which allow us to study non-isotropic effects, still under homegeneity assumptions. Finally we briefly describe the quasi-homogeneous model, which is necessary if we wish to include spatial variations of the intensity of the turbulence.

3.1 The von Karman spectrum

The von Karman spectrum is given by

$$\Phi(K) = 0.033\, C_n^2 (K^2 + L_0^{-2})^{-11/6} \exp(-K^2/K_m^2) \qquad (10)$$

where

$$K_m = \frac{5.92}{l_0} \qquad (11)$$

and C_n is the structure constant, which is a measure of the strength of the turbulence. The inner scale l_0 is the eddy size below which turbulent energy is assumed to dissipate into heat. It is usually taken to be of the order of a millimetre. The outer scale L_0 gives the maximum size for eddies contributing to locally homogeneous turbulence, and is usually taken to be of the order of 10 metres. In the inertial subrange $l_0 \le K \le L_0$, the von Karman spectrum is a good approximation to the Kolmogorov spectrum which describes atmospheric turbulence assuming local homogeneity.

We first note that for any positive integer p, the von Karman spectrum satisfies

$$\int_{\mathbb{R}^3} |\mathbf{K}|^{2p} \Phi(\mathbf{K}) d\mathbf{K} < \infty \qquad (12)$$

Hence from theorem 2, the sample paths are indefinitely differentiable with probability 1, and we can use Maxwell's equations for a smoothly varying medium. In order to see if the parabolic approximation is valid in the turbulent atmosphere, we need to estimate the refractive index gradients. The crucial parameters are the variances $\sigma_x^2, \sigma_y^2, \sigma_z^2$ of the partial derivatives of n_f. We have

$$\sigma_x^2 = \left\langle \left(\frac{\partial n_f}{\partial x} \right) \right\rangle$$

$$= \left\langle \lim_{h \to 0} \left(\frac{n_f(x+h,y,z,) - n_f(x,y,z)}{h} \right)^2 \right\rangle$$

$$= \lim_{h \to 0} \left\langle \left(\frac{n_f(x+h,y,z,) - n_f(x,y,z)}{h} \right)^2 \right\rangle \qquad (13)$$

$$= \lim_{h \to 0} \frac{2}{h^2} \left(B(0,0,0) - B(x,0,0) \right)$$

$$= -\frac{\partial^2 B}{\partial x^2}(0,0,0)$$

From the Wiener-Khintchine representation, we can write

$$-\frac{\partial^2 B}{\partial x^2}(0,0,0) = \int_{\mathbb{R}^3} K_x^2 \, \Phi(\mathbf{K}) d\mathbf{K} \qquad (14)$$

We note that for an isotropic spectrum, all the partial derivatives have the same variance σ^2. For the von Karman spectrum, we obtain after some algebra

$$\sigma^2 = \frac{\pi}{\Gamma\left(\frac{3}{2}\right)} \times 0.033 \, C_n^2 \, K_m^{4/3} \int_{L_0^{-2}}^{\infty} v^{-1/3} e^{-v} \psi\left(3/2, 2/3, v\right) dv \qquad (15)$$

where ψ is the confluent hypergeometric function or Kummer function [1]. We get a bound on σ by writing

$$\sigma^2 \leq 0.033 \, \pi \, C_n^2 \, K_m^{4/3} \int_0^{\infty} \int_0^{\infty} v^{-1/3} e^{-v} u^{1/2} (1+u)^{-11/6} e^{-uv} du \, dv$$

$$\leq 0.033 \, \pi \, C_n^2 \, K_m^{4/3} \int_0^{\infty} \int_0^{\infty} v^{-1/3} e^{-v} (1+u)^{-4/3} du \, dv$$

$$\qquad (16)$$

$$= 3\Gamma(2/3) \times 0.033 \, \pi \, C_n^2 K_m^{4/3}$$

$$= 4.56 \, C_n^2 \, l_0^{-4/3}$$

Hence the variance of the refractive index gradient increases with the strength of the turbulence and with the inverse of the inner scale l_0: the presence of significant energy in small eddies tends to make the refractive index profiles more irregular.

It follows from equation 7 that on average the partial derivatives of the refractive index have a modulus greater than 10σ in a proportion of less than 1.524×10^{-23} of the volume of interest, small enough to be neglected. If we take $l_0 = 10^{-3}$ m, and $C_n = 10^{-7}\,\mathrm{m}^{-1/3}$, a value typical of strong turbulence, we have

$$\sigma \le 2.14 \times 10^{-5}\,\mathrm{m}^{-1} \tag{17}$$

Hence on average, we can assume that the partial derivatives of the refractive index have a modulus less than $2.14 \times 10^{-4}\,\mathrm{m}^{-1}$ in all but a negligible proportion of the domain of interest. For radar frequencies of interest, wavelengths range from a few millimetres to a few metres and these gradients remain small on the scale of a wavelength. We conclude that the parabolic approximation is valid even in extremely strong atmospheric turbulence.

Since the quantity accessible to measurements is the variance of the refractive index fluctuations, it is useful to find a relationship between $\langle n_f^2 \rangle$ and C_n^2. For the von Karman spectrum, the variance of the refractive index fluctuations is linked to the structure constant C_n^2 by [9]

$$\langle n_f^2 \rangle = 0.52\, C_n^2 L_0^{2/3} \tag{18}$$

Table 1 gives typical values for weak, medium and strong atmospheric turbulence, taking $L_0 = 10$ m.

Table 1: Structure constant and standard deviation of refractive index fluctuations

	C_n^2	$\sqrt{\langle n_f^2 \rangle}$
weak turbulence	$10^{-18}\,\mathrm{m}^{-2/3}$	1.55×10^{-9}
medium turbulence	$10^{-16}\,\mathrm{m}^{-2/3}$	1.55×10^{-8}
strong turbulence	$10^{-14}\,\mathrm{m}^{-2/3}$	1.55×10^{-7}

We see that turbulence would have to be exceptionally strong for the refractive index standard deviation to reach values of $10-6$, and the refractivity fluctuations tend to remain less than a fraction of an N-unit.

3.2 The Gaussian spectrum

For theoretical studies, it is often very convenient to use a Gaussian correlation function of the form

$$B_n(x, y, z) = \sqrt{\langle n_f^2 \rangle}, \exp\left(-\frac{x^2}{L_x^2} - \frac{y^2}{L_y^2} - \frac{z^2}{L_z^2}\right) \tag{19}$$

Here the process is not isotropic, since the correlation lengths L_x, L_y, L_z are not necessarily equal. The correlation function is infinitely differentiable, and hence so are the sample paths with probability one. The variances of the refractive index partial derivatives are given by

$$\sigma_s = \frac{\sqrt{2}}{L_s}\sqrt{\langle n_f^2 \rangle}, \quad s = x, y, z \tag{20}$$

Typical values of $\sqrt{\langle n_f^2 \rangle}$ in very strong turbulence would be at most of the order of 10^{-6}, giving σ_s of the order of $\sqrt{2} \times 10^{-6}/L_s$. Even for very strongly correlated turbulence, for example taking $L_s = 1$ cm, the variances of the refractive index gradients are still of the order of $10^{-4}\,\mathrm{m}^{-1}$ and the parabolic approximation is valid for the frequencies of interest.

3.3 Quasi-homogeneity

In general, the variance of the refractive index fluctuations is a function of space, and the turbulence process is not homogeneous, nor even locally homogeneous. Following [10, 19], we use a weighted homogeneous model for the random refractive index, writing

$$n_f(\mathbf{r}, \omega) = \sqrt{\langle n_f^2(\mathbf{r}) \rangle}\, X(\mathbf{r}, \omega) \tag{21}$$

where the process X is homogeneous.

We note here that although there are turbulence models for the boundary layer [7], very little is known about turbulent structures in the free atmosphere. In particular there is much speculation about the so-called "collapse problem" of 3D turbulence, and it has been postulated that turbulent eddies in a stably stratified atmosphere might well be pancake-shaped, with correlation lengths much larger in the horizontal than in the vertical [12]. We shall see later that non-isotropy may have important consequences for radar propagation. The problem of deriving vertical profiles for the variations of $\sqrt{\langle n_f^2(x + \Delta x/2, z) \rangle}$ in the free atmosphere is linked to this description in terms thin turbulent layers ations. The

8

VanZandt model [25], which computes an average C_n^2 profile from radiosonde ascent data, could prove extremely useful in that respect. We note however that this would not address the problem of horizontal correlation.

4 PE solution for one realisation

It follows from the previous section that realisations of the refractive index fluctuations are sufficiently regular to justify the use of the parabolic approximation. In fact, the variations of the refractive index are sufficiently slow on the scale of a wavelength to justify the use of the split-step solution of the narrow-angle parabolic equation [11]. One caveat is that our application can involve relatively large heights relative to the Earth surface. Accurate modelling requires a conformal Earth flattening transformation with a modified refractive index [11] defined by

$$m(x, z) = n(x, z) \exp\left(z/a\right) \tag{22}$$

where a is the Earth radius, x corresponds to the ground range and $z = a \log(1 + h/a)$ is a logarithmic function of the height h above the Earth surface.

Let $u(x, z)$ be the reduced PE field. Assume first that there is no air/ground interface at the bottom of the domain. Then the split-step solution is given by

$$u(x + \Delta x, z) = \exp\left(\frac{ik}{2} \int_x^{x+\Delta x} (n^2(\xi, z) - 1)d\xi\right)$$
$$\times \int_{-\infty}^{\infty} u(x, z')e^{ik(z-z')^2/2\Delta x}dz' \tag{23}$$

The convolution integral is calculated numerically with a Fast Fourier Transform. In the presence of the air/ground interface, boundary conditions are enforced by replacing the convolution integral with a more complicated expression, which is implemented numerically with a sine transform or mixed transform [5]. We then have a solution of the form

$$u(x + \Delta x, z) = \exp\left(\frac{ik}{2} \int_x^{x+\Delta x} (n^2(\xi, z) - 1)d\xi\right) F(u(x, \cdot)) \tag{24}$$

where F depends only on the field at previous ranges. The main point to bear in mind is that refractive index variations on the interval $[x, x+\Delta x]$ only intervene in the exponential factor.

9

In order to solve the split-step equation, we have to generate a realisation of the integrated random fluctuations of the refractive index over the range interval $[x, x + \Delta x]$. Since n is close to unity, we make the approximation

$$\frac{n^2 - 1}{2} \sim n_d + n_f \tag{25}$$

We note that since we are neglecting propagation effects in the transverse direction y, we only require the behaviour of the correlation function for points with the same value of y. The random process of interest then represents the integrated phase fluctuations

$$\nu(x, z) = \int_x^{x+\Delta x} n_f(\xi, 0, z) \, d\xi \tag{26}$$

We now look at the autocorrelation function of the process $\nu(, x, z)$.

5 Computing B_ν

If n_f is homogeneous, the autocorrelation function B_ν of ν is given by

$$B_\nu(x, z) = \int_0^{\Delta x} \int_0^{\Delta x} B_n(x + x_2 - x_1, y, z) dx_1 dx_2 \tag{27}$$

Making the change of variable $s = x_2 - x_1, t = x_1$, we obtain

$$B_\nu(x, z) = \int_0^{\Delta x} (\Delta x - s)(B_n(x + s, 0, z) + B_n(x - s, 0, z)) ds \tag{28}$$

In particular this yields for $x = 0$

$$B_\nu(0, z) = \Delta x \int_{-\Delta x}^{\Delta x} B_n(s, 0, z) ds - \int_{-\Delta x}^{\Delta x} |s| B_n(s, 0, z) ds \tag{29}$$

and for any positive integer j, the inequality

$$B_\nu(j\Delta x, 0, z) \leq \Delta x \int_{\Delta x}^{\infty} B_n(s, 0, z) ds + \int_0^{\Delta x} s B_n((j-1)\Delta x + s, 0, z)) ds \tag{30}$$

10

5.1 Uncorrelated phase-screens

Suppose that we have

$$\int_{\Delta x}^{\infty} B_n(s,0,z)ds \ll \int_0^{\Delta x} B_n(s,0,z)ds \tag{31}$$

and

$$\int_0^{\Delta x} sB_n(s,0,z)ds \ll \Delta x \int_0^{\Delta x} B_n(s,0,z)ds \tag{32}$$

Then we can make the approximations

$$B_\nu(0,z) \sim \Delta x \int_{-\infty}^{\infty} B_n(s,0,z)ds \tag{33}$$

and

$$B_\nu(j\Delta x, z) \sim 0 \tag{34}$$

when j is a positive integer. Equation 34 means that the phase screens are approximately uncorrelated, while Equation 33 is simply a convenient approximation which is consistent with Equation 34. Equation 34 is a form of the Markov approximation (see section 6 below).

Approximations 33 and 34 are good when the range step Δx is much larger than the range correlation length L_x, which is often the case in practice. For example with the Gaussian correlation function given by equation 19, using a first order asymptotic expansion for the complementary error function [1], we obtain if $L_x \ll \Delta x$

$$B_\nu(0,z) \sim \left(\sqrt{\pi}L_x\Delta x - L_x^2\right)\exp(-z^2/L_z^2) \tag{35}$$

for the correlation between points at the same range, while the correlation between successive screens satisfies

$$B_\nu(\Delta x, z) \sim \frac{L_x^2}{2}\exp(-z^2/L_z^2) \tag{36}$$

11

Since we have

$$B_\nu(\Delta x, z) \ll B_\nu(0, z) \tag{37}$$

it is tempting to assume that the screens are uncorrelated. We can then take

$$B_\nu(0, z) \sim \sqrt{\pi} L_x \Delta x \exp(-z^2/L_z^2) \tag{38}$$

If we neglect the correlation between the screens, the relative error on the correlation function is of the order of $L_x/\Delta x$ at each step. Typical values of $\Delta x/L_x$ are of the order of 10 to 100, and the relative error on the correlation function of the phase screens at each step will range from 1% to 10%. This could clearly lead to large cumulative errors for simulations requiring hundreds of steps, which is the case for the airborne radar application.

The error analysis performed in [22, 23] shows the effect of the range step on accuracy of the moments of the field when the phase screens are modelled with the appropriate range correlation, assuming the range step is less than the correlation length. The work of Rouseff shows that excellent results are achieved for independent phase screens when the range step is much larger than the correlation length, at least at relatively short ranges. However these publications do not address the issue of cumulative error at very large ranges, and in particular the effect of the Markov approximation. The work of Dashen [4] indicates that the Markov approximation is likely to be inaccurate for non-homogeneous media.

5.2 Correlated phase-screens

If we do not make the approximation that the phase screens are uncorrelated, we can generate accurate realisations of the phase screens by writing the correlation function as

$$B_\nu(x, z) = (x + \Delta x) \int_x^{x+\Delta x} f(s)ds - (x - \Delta x) \int_{x-\Delta x}^x f(s)ds \\ + \int_{x-\Delta x}^x sf(s)ds - \int_x^{x+\Delta x} sf(s)ds \tag{39}$$

where $f(s) = B_n(s, 0, z)$. Differentiating twice with respect to x, we get

$$\frac{\partial^2 B_\nu}{\partial x^2}(x, z) = f(x + \Delta x) + f(x - \Delta x) - 2f(x) \tag{40}$$

Using the Fourier transform theorems for derivatives, we obtain

$$B_\nu(x, z) = \int_{-\infty}^{\infty} \frac{4 \sin^2(K_x \Delta x)/2}{K_x^2} e^{iK_x x} \int_{-\infty}^{\infty} B_n(s, 0, z) e^{-iK_x s} ds\, dK_x \tag{41}$$

This takes a particularly simple form when the correlation function B_n is Gaussian: the spectrum ϕ_ν is then given by

$$\Phi_\nu(K_x, K_z) = L_x L_z \frac{2 \sin^2(K_x \Delta x/2)}{K_x^2} e^{-(K_x^2 L_x^2 + K_z^2 L_z^2)/4} \tag{42}$$

5.3 Frozen-in-range turbulence

In the extreme case where the turbulence depends on height only, the phase-screens do not depend on range and we have

$$B_\nu(x, z) = (\Delta x)^2 B_n(0, 0, z) \tag{43}$$

For this case, it is sufficient to generate one height-dependent phase screen which is kept constant throughout the marching procedure, using the normalisation of equation 43

5.4 Quasi-homogeneity

If n_f is only quasi-homogeneous, but exhibits slow variations of the variance with range, it is straightforward to extend these results by noting that the integrated phase fluctuations are approximately quasi-homogeneous, with

$$\nu(x, z) \sim \sqrt{\langle n_f^2(x + \Delta x/2, z)\rangle} \int_x^{x+\Delta x} X(\xi, 0, z) d\xi \tag{44}$$

We can then generate realisations of ν as follows: we first obtain realisations of the homogeneous process $Y = \int_x^{x+\Delta x} X(\xi, 0, z) d\xi$ using the Wiener-Khintchine spectral representation, and then multiply by the refractive index standard deviation $\sqrt{\langle n_f^2(x + \Delta x/2, z)\rangle}$.

5.5 Numerical implementation

The Monte-Carlo approach requires a very good random number generator, since very large numbers of calls are required. Here we have used the random generator of L'Ecuyer [18] with period 2.3×10^{18}, which provides random numbers sequences of excellent statistical quality for lengths up to 10^{17} or so. Even for very large AWACS simulations with a vertical FFT size of 65536 and 1000 range steps, the total number of calls for a set of 250 simulations is of the order of 10^9, which is far below the reliability theshold of the L'Ecuyer generator.

It is straightforward to generate independent phase-screens with the appropriate height correlation, using a discrete version of the Wiener-Khintchine spectral representation [13]. Things become more difficult however if we wish to model range correlation. The spectral approach then requires a large two-dimensional FFT, since accurate representation of the spectrum requires a spatial step size which is small compared to the correlation length of the medium. For this reason most authors assume independence of the phase-screens.

6 Moment equations

For many years, researchers have attempted to derive and solve partial differential equations for the moments of the fields. This is only possible under the Markov approximation, which assumes that the field at range $x + \Delta x$ does not depend on refractive index fluctuations at ranges less than x. It has been shown in [4] that this is an excellent assumption when the turbulence is homogeneous and isotropic, with a a scale size small compared to the range step. The moment equations have been derived by Tatarski [24] for the case of a homogeneous isotropic medium which is delta-correlated in range, and by Mandine [14] under slightly more general assumptions using the stochastic integral formalism. Here we derive them directly from the split-step parabolic equation under the Markov approximation.

The Markov approximation can be stated as follows: we assume that for any range x, any distinct integers j_1, j_2 and any heights z_1, z_2, the random variable $\nu(x + j_1 \Delta x, z_1)$ which represents the integrated fluctuations of the refractive index at height z_1 between ranges $x + j_1 \Delta x$ and $x + (j_1 + 1)\Delta x$ is independent of $\nu(x + j_2 \Delta x, z_2)$. Then we can revisit equation 24 to compute the successive moments of the field. Using approximation 25 together with the Markov approximation, we have for the first moment

$$\langle u(x + \Delta x, z) \rangle = e^{ik\Delta x n_d(x + \Delta x/2, z)} \left\langle e^{ik\nu(x,z)} \right\rangle \langle F(u(x, \cdot)) \rangle \tag{45}$$

Since the refractive index process is Gaussian, we have

$$\left\langle e^{ik\nu(x,z)}\right\rangle = e^{-k^2\left\langle \nu^2(x,z)\right\rangle/2} \tag{46}$$

For a quasi-homogeneous process with slow variations in range, this becomes approximately

$$\left\langle e^{ik\nu(x,z)}\right\rangle = e^{-k^2\left\langle n_f^2(x+\Delta x/2,z)\right\rangle B_X(0,z)/2} \tag{47}$$

Since F is linear, we also have

$$\langle F(u(x,\cdot))\rangle = F(\langle u(x,\cdot)\rangle) \tag{48}$$

Putting $M_1(x,z) = \langle u(x,z)\rangle$, and $A_0(x,z) = \left\langle \nu^2(x,z)\right\rangle$, we see that the first moment M_1 satisfies

$$M_1(x+\Delta x,z) = e^{ik\Delta x\, n_d(x+\Delta x/2,z)}\, e^{-k^2 A_0(x,z)/2} F(M_1(x,\cdot)) \tag{49}$$

This directly provides a marching solution for the first moment. We see that the effect of turbulence on the first moment is to absorb some of the energy of the field with a height and range dependent absorptive term.

Equations for higher moments are obtained in a similar way from the split-step solution of the parabolic equation together with the Markov approximation. For example the second moment equation is of the form

$$M_2(x+\Delta x,z_1,z_2) = e^{ik\Delta x[n_d(x+\Delta x/2,z_1)-n_d(x+\Delta x/2,z_2)]} \tag{50}$$

$$e^{-k^2 A_2(x,z_1,z_2)/2} G(M_2(x,\cdot,\cdot))$$

where

$$M_2(x,z) = \left\langle u(x+\Delta x,z_1)u(x+\bar{\Delta} x,z_2)\right\rangle$$

$$A_2(x,z_1,z_2) = \left\langle (\nu(x,z_1)-\nu(x,z_2))^2\right\rangle$$

The linear functional G depends on boundary conditions at the ground. For example if there is no ground interface, we have

$$Gf(x, z_1, z_2) = \int_{\mathbb{R}^2} g(x, z_1', z_2') e^{ik[(z_1-z_1')^2-(z_2-z_2')^2]/2\Delta x} dz_1' dz_2' \qquad (51)$$

A few comments are in order at this stage. We first note that the first moment equation is computationally equivalent to the PE for a single realisation, with only a very small overhead for the computation of the absorptive exponential term. The first moment is however of little use when examining the effects of turbulence on radar or communications systems: the main effects arise from the fluctuations of the field. These give rise to scintillation phenomena which degrade target tracking or signal reception. The second moment gives information on the mutual coherence of the field, while the fourth moment gives information on the intensity fluctuations of the field, and those are the more relevant quantities to study.

Now the fourth moment equation involves four independent height variables and cannot be handled numerically except for very small problems. Approximations can be made to obtain more tractable equations [9, 13], but very few numerical results are available. The second moment equation involves two independent height variables and its numerical solution requires two-dimensional FFTs. Although this approach is not out of the question, we notice that it is not actually cheaper than the Monte-Carlo approach: Rouseff [19] obtained reliable second and fourth moment estimates with 250 simulations. Now if the vertical FFT size is greater than 256, this is a cheaper way to obtain the second moment than solving the second moment equation, and of course vertical FFT sizes for airborne problems are orders of magnitudes larger than 256. If we consider that the Monte Carlo approach does not require the Markov approximation, and will yield good estimates of both the second and the fourth order moments, we may conclude that the Monte-Carlo approach is both more efficient and more accurate than the moment equations.

7 Application to airborne sensors

7.1 10 GHz example

In this section, we look at a generic helicopter case, with a 10 GHz horizontally polarised source at an altitude of 1500 m. The beamshape of the antenna is Gaussian, with a half-power beamwidth of 1° and an elevation of −0.15°. The parabolic equation simulations for this case use a range step of 250 m, a height step of 25 cm and a sine transform size of 16384. Figures 1 and 2 show the antenna coverage in standard conditions (exponential atmosphere) and when an elevated duct is present. The modified refractive index profile for the duct is given in Table 2: the ducting layer is located between 500 and 600 m.

16

Table 2: Elevated duct profile for 10 GHz simulations

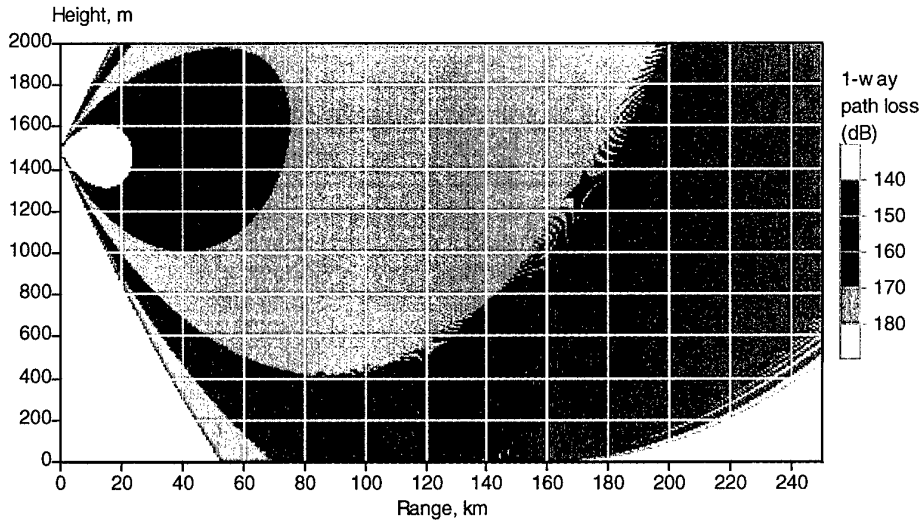| Height (m)	Modified refractivity (M-units)
0	330
500	390
600	380
1600	498

Figure 1: Airborne X-band antenna in standard atmosphere.

The parabolic equation simulations use the discrete mixed transform of [5] to model impedance boundary conditions at the ground, together with a ray-trace algorithm to find a representative grazing angle at each range. With this model, we can take roughness effects into account. Here we assume propagation over a rough sea surface, using the Miller model [15] to compute the effective reflection coefficient and the Phillips isotropic sea surface spectrum [17] which gives the rms waveheight as a function of wind speed. The wind speed is 10 m/s, corresponding to average roughness conditions. The rms wave height for this wind speed is 0.51 m. The roughness inhibits lobing, except at the shallower grazing angles. When the duct is present, a very marked radar hole appears as expected. Figure 3 shows path loss again against height at a range of 250 km for the two refractivity environments. The signal is enhanced close to the surface and just above the duct due to partial trapping of the reflected energy and to scattering from the duct, and there is a substantial decrease in the radar hole, where the signal is 10 to 15 dB below its standard value.

Height, m
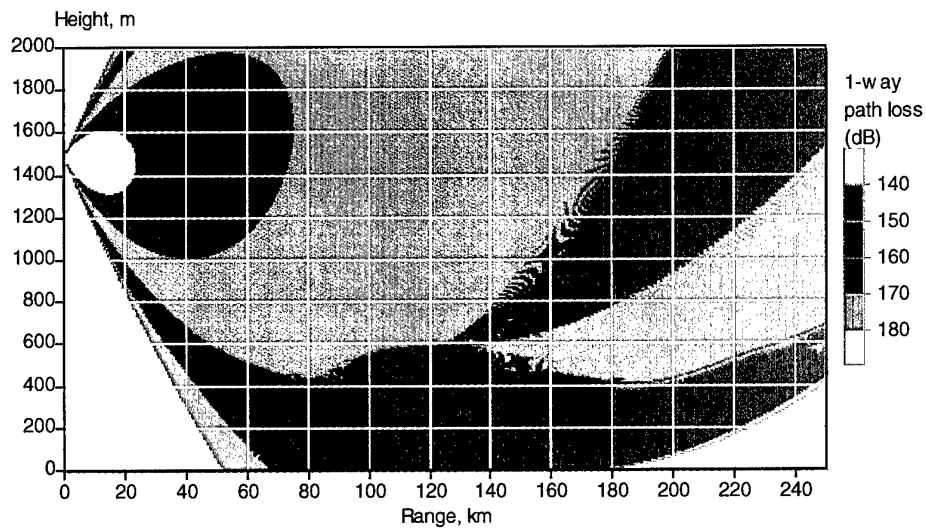
Figure 2: Airborne X-band antenna in elevated duct of Table 2.

Vertical path

———— standard atmosphere ———— duct
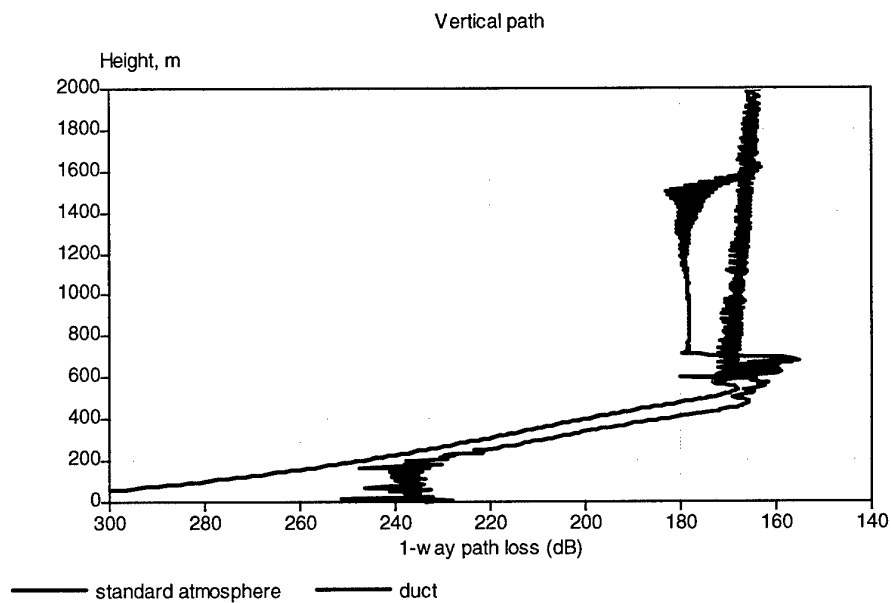
Figure 3: Comparison of X-band signal at range 250 km in standard atmosphere and elevated duct.

We now look at turbulence effects on the radar hole. The random profile generator can deal with arbitrary variations of the refractive index variance, which means there is considerable flexibility for the simulations. Here we show results for the $\sqrt{\langle n_f^2 \rangle}$ profile of Table 3, which exhibits stronger turbulence inside the layer, and for a constant profile with $\sqrt{\langle n_f^2 \rangle} = 0.5 \times 10^{-6}$. Naturally these values correspond to extremely strong turbulence which may not occur in reality. Linear interpolation is used to compute the turbulence profile between the data points.

Table 3: Turbulence profile for 10 GHz simulations

Height (m)	$\sqrt{\langle n_f^2 \rangle}$ (N-units)
0	0.1
500	0.1
550	0.5
600	0.1
1600	0.1

Figures 4 and 5 show path loss contours respectively for the turbulence profile of Table 3 and for uniform very strong turbulence. For both of these simulations, the von Karman spectrum has been used to generate the random refractive index structure, with the outer scale L_0 set to 10 m. Here we assume independent phase-screens.

Although the variable turbulence profile does increase the variability of the field at short ranges, we have to go the the very strong uniform turbulence to see effects at longer ranges. This is confirmed by Figure 6, which shows increased fluctuations in the radar hole for the uniform turbulence case. Even with this very strong turbulence environment, the effects are relatively small. We also see increased scatter close to the surface. In view of the very weak signal strength values, this is unlikely to have operational significance.

We now consider a Gaussian correlation function in order to look at the effects of the horizontal correlation length. For the simulations that follow, the turbulence is uniform, with $\sqrt{\langle n_f^2 \rangle} = 0.5 \times 10^{-6}$. Figures 7, 8 and 9 correspond respectively to isotropic turbulence ($L_x = L_z = 10$ m), non-isotropic turbulence ($L_x = 100$ m, $L_z = 10$ m), and frozen-in-range turbulence ($L_x = \infty$, $L_z = 10$ m), where the random fluctuations depend on height only. For the non-isotropic case, the ratio $L_x/\Delta x$ is equal to 0.4, and the assumption of independent phase screens is acceptable. For the frozen-in-range case, we keep the same phase-screen throughout, using the results of section 5.3.

Results for the isotropic Gaussian spectrum are very similar to those for the von Karman spectrum, but there are considerables changes as the horizontal correlation length increases. Then as the irregularities in the refractive index profile persist in range, they give rise to multiple thin ducting layers which can have long-range effects. This becomes particularly striking for the frozen-in-range case. Figure 10 shows path loss against height
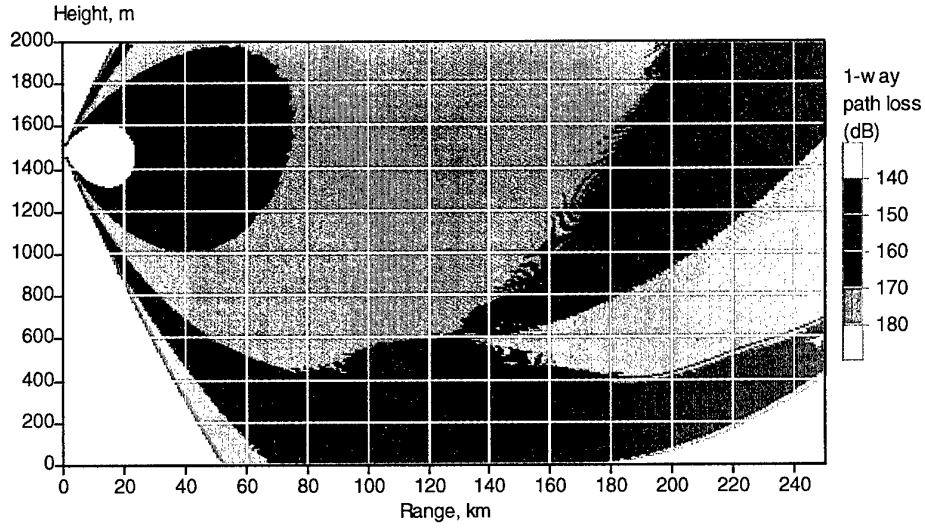
19

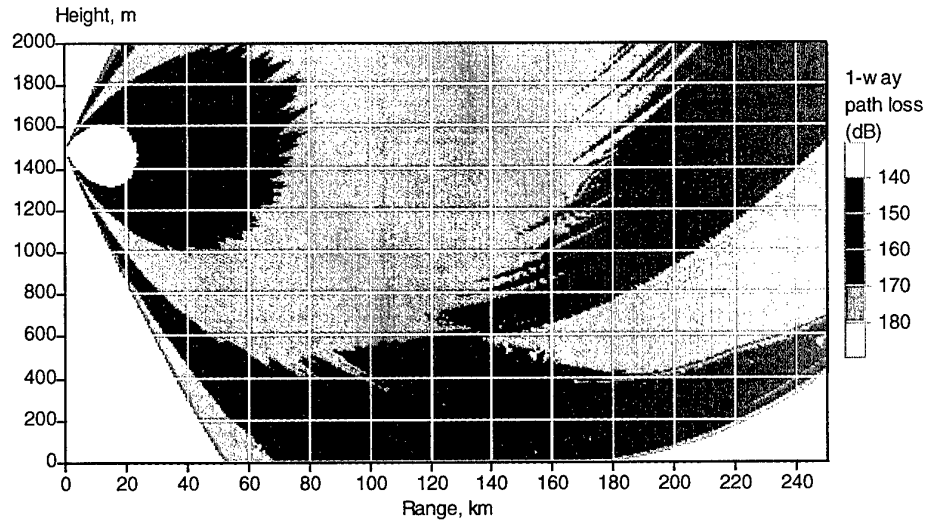Figure 4: Airborne X-band antenna in elevated duct, von Karman spectrum with turbulence profile of Table 3.

Figure 5: Airborne X-band antenna in elevated duct, von Karman spectrum with uniform turbulence, $\sqrt{\langle n_f^2 \rangle} = 0.5 \times 10^{-6}$, $L_0 = 10$ m.
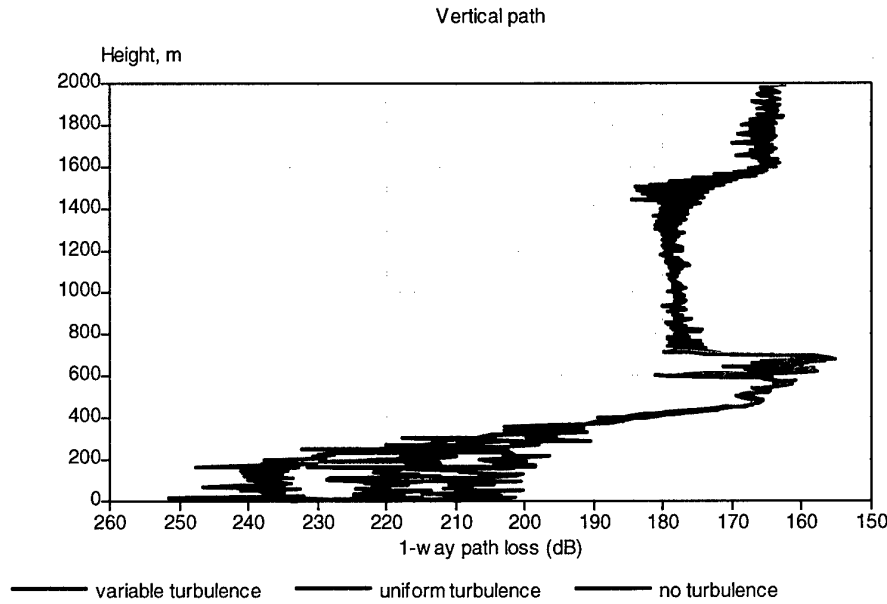
Vertical path

Height, m

Figure 6: Comparison of X-band signal at range 250 km in elevated duct with variable and uniform turbulence (von Karman spectrum, turbulence profile of Table 4) and without turbulence.

at a range of 250 km for the frozen-in-range case, the non-isotropic turbulence case and the reference ducting environment without turbulence. Fluctuations are much more severe here than in the isotropic case, reaching values well over 10 dB. The frozen-in-range case also leads to much increased signal values close to the ground. It is interesting to note that for this case the non-isotropic turbulence actually strengthens the radar hole at heights between 800 and 1000 m or so.

7.2 AWACS example

We now consider a 3 GHz horizontally polarised source at an altitude of 9000 m. The beamshape of the antenna is Gaussian, with a half-power beamwidth of 3° and an elevation of $-0.25°$. The parabolic equation simulations for this case use a range step of 500 m, a height step of 30 cm and a sine transform size of 65536. Figures 11 and 12 show the antenna coverage in standard conditions (exponential atmosphere) and with the elevated duct environment given in Table 4. This is a very strong ducting layer with an M-deficit of 20 M-units, located between altitudes of 1500 and 1600 m. When the duct is present, a radar hole opens at a range of 300 km or so.

Here we have used the same rough surface model as in the previous section, with a wind speed of 10 m/s at the shallower grazing angles. We note that the surface roughness does not inhibit high altitude lobing at this frequency. We can look at the effects in more detail
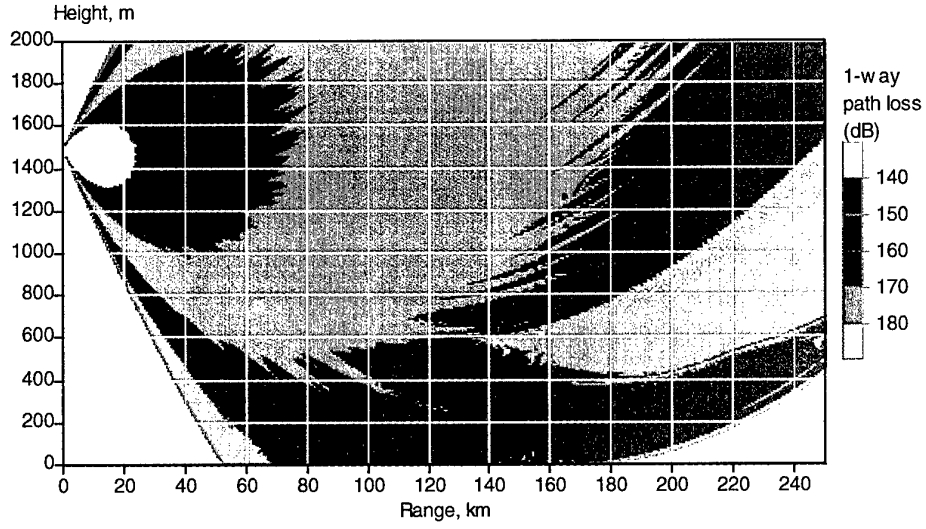
Figure 7: Airborne X-band antenna in elevated duct, isotropic Gaussian spectrum, $L_x = L_z = 10$ m.
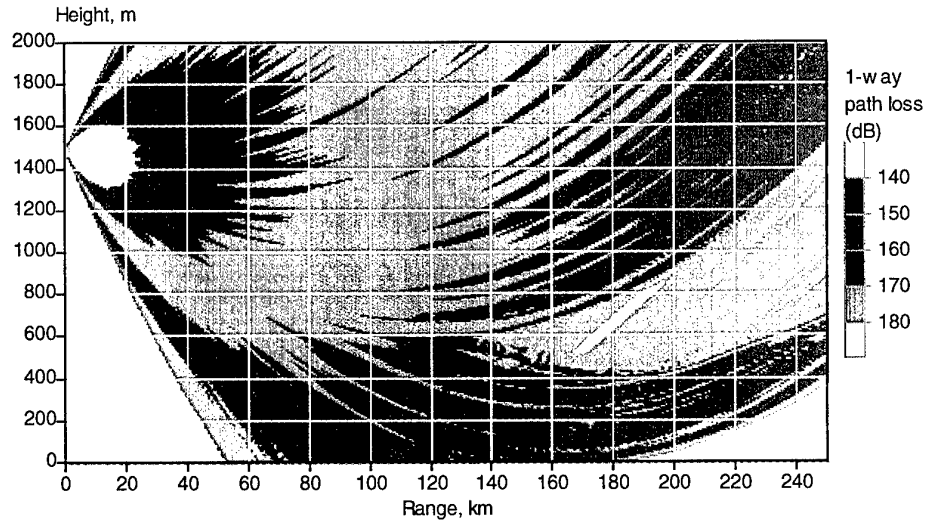

Figure 8: Airborne X-band antenna in elevated duct, non-isotropic Gaussian spectrum, $L_x = 100$ m, $L_z = 10$ m.
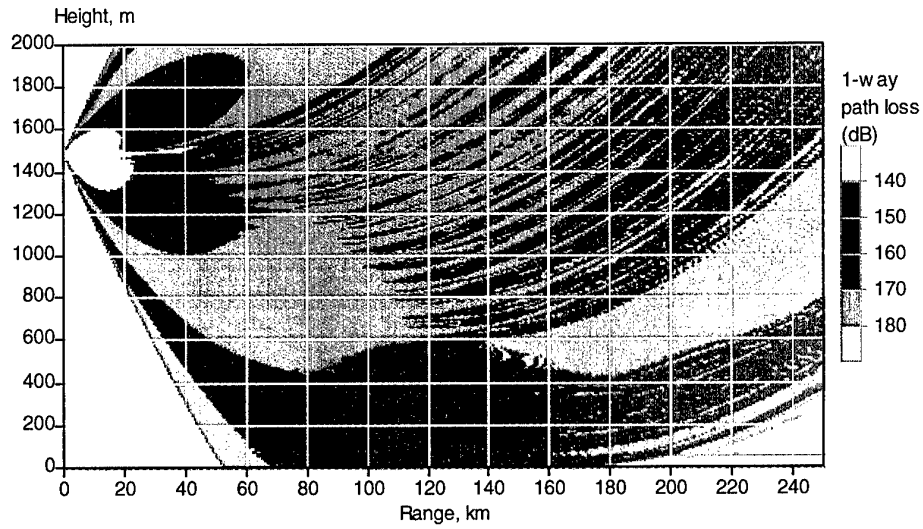
Figure 9: Airborne X-band antenna in elevated duct, frozen in range turbulence, Gaussian spectrum, $L_z = 10$ m.
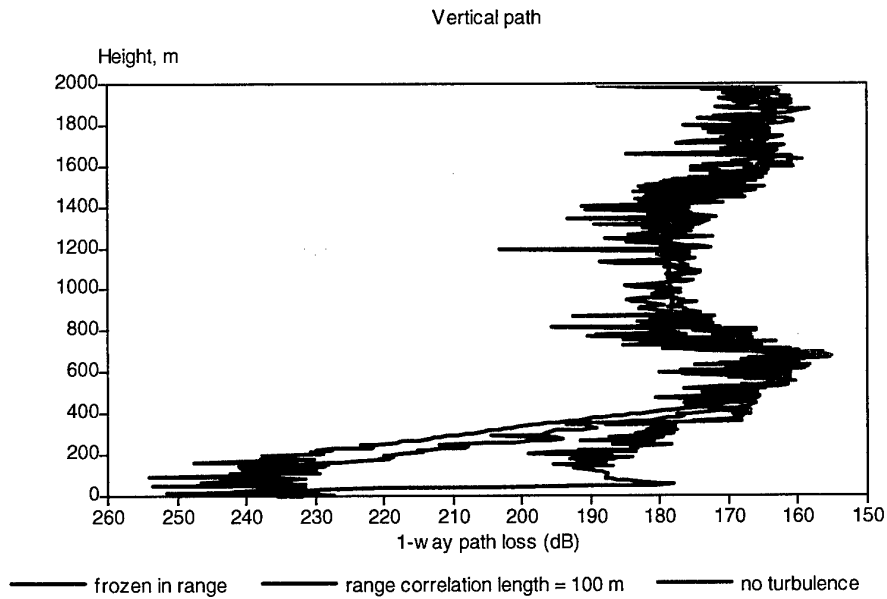

Figure 10: Comparison of X-band signal at range 250 km in elevated duct with frozen in range and non-isotropic turbulence (Gaussian, turbulence profile of Table 4) and without turbulence.

23

Table 4: Elevated duct profile for AWACS simulations.

Height (m)	Modified refractivity (M-units)
0	325
1500	500
1600	480
2600	598
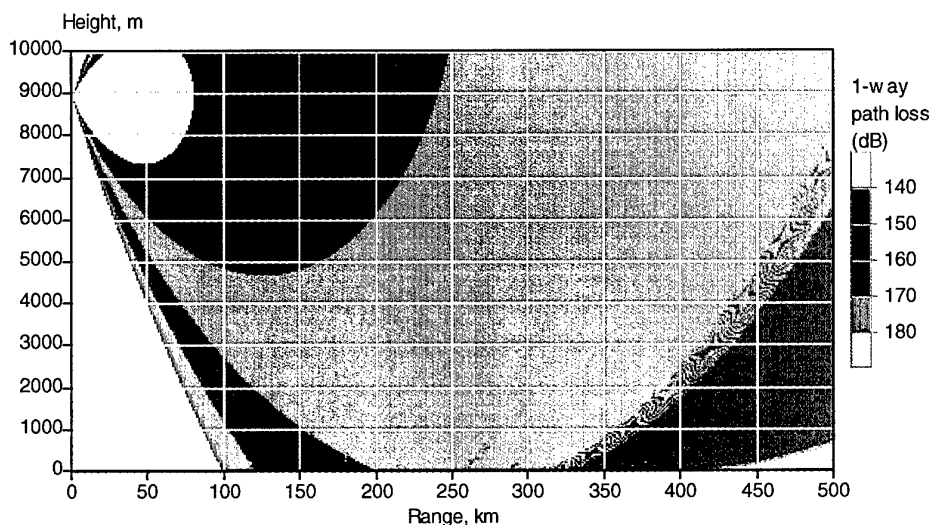
Figure 11: AWACS coverage in standard atmosphere.

in Figure 13, which shows path loss again against height at a range of 500 km for the standard and ducting environments. The hole is quite pronounced, with a drop of almost 10 dB compared to the envelope of the signal in the standard case.

We now look at turbulence effects. Figure 14 shows the coverage in a turbulence atmosphere modelled with the von Karman spectrum. The turbulence is uniform, with the extremely high value $\langle n_f^2 \rangle = 0.5 \times 10^{-6}$ for the refractive index fluctuations. This does give rise to fluctuations in the signal, as shown in Figure 15, but the variability remains small even in this very strong turbulence, and there is litlle impact on the radar hole. We have to consider non-isotropic turbulence in order to see more substantial effects. Figures 16 and 17 show path loss contours respectively for a non-isotropic Gaussian spectrum with $L_x = 500$ m and for the frozen-in-range case. For both simulations we have taken $L_z = 10$ m and $\langle n_f^2 \rangle = 0.5 \times 10^{-6}$. Turbulence effects then become very severe, with numerous small ducting layers partially destroying the coherence of the overall elevated duct trapping.
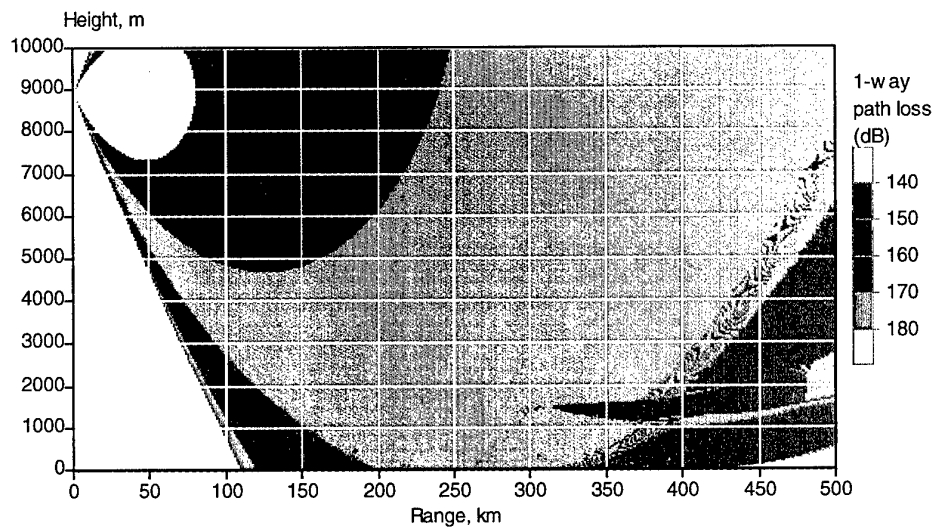
24

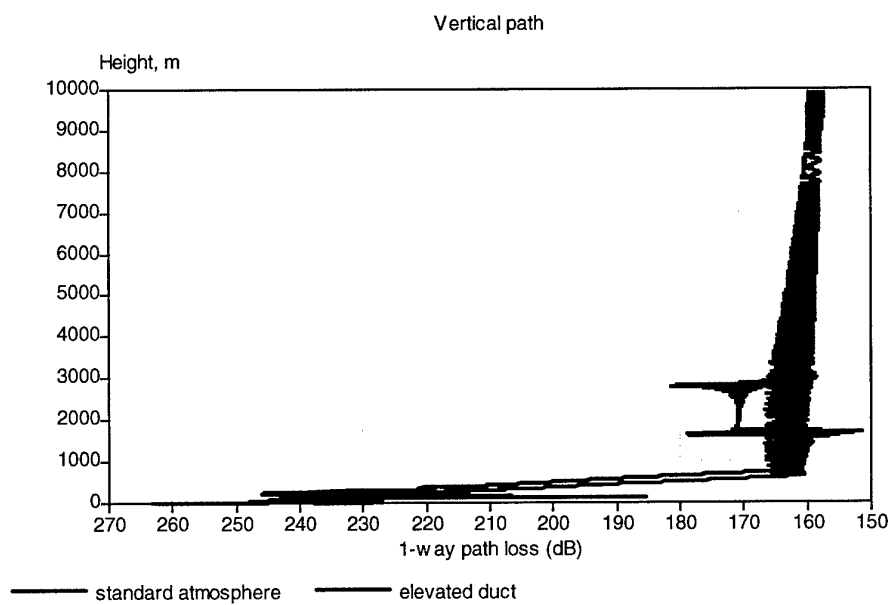Figure 12: AWACS coverage in elevated duct of Table 3.

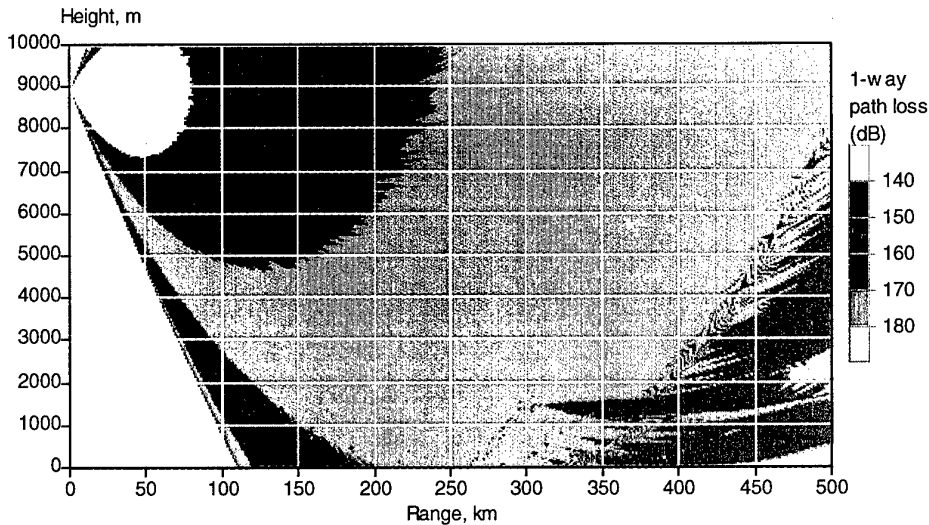Figure 13: Comparison of AWACS signal at range 500 km in standard atmosphere and elevated duct.

Figure 14: AWACS coverage, von Karman spectrum with $\langle n_f^2 \rangle = 0.5 \times 10^{-6}$, $L_0 = 10$ m.

Figures 18 and 19 show these effects in more detail at range 500 km. We note that even in these very severe conditions, the radar hole is still quite effective, although both the spatial extent and the signal drop have been reduced.

8 Conclusions and future work

We have demonstrated in this report that parabolic equation models are adequate for simulations of radar propagation in atmospheric turbulence. This has been achieved by showing that if we assume the turbulent processes are quasi-homogeneous and Gaussian, the most commonly used spectra lead to very weak refractive index gradients for individual realisations, even in strong turbulence. Under the Markov approximation, we have derived parabolic equation solutions for the moments of the field in a particularly simple fashion which avoids the use of stochastic integrals. However beyond the first order, which is of little interest for radar applications, the moment equations are more expensive computationally than Monte-Carlo simulations, which have the added advantage of not requiring the Markov approximation.

Monte-Carlo parabolic equation simulations involve the generation of random phase-screens to represent the integrated refractive index fluctuations over a range step. Formulae for the correlation functions for the integrated fluctuations have been given, both in the general case and in the case where the phase-screens can be treated as uncorrelated in range, corresponding to the Markov approximation.
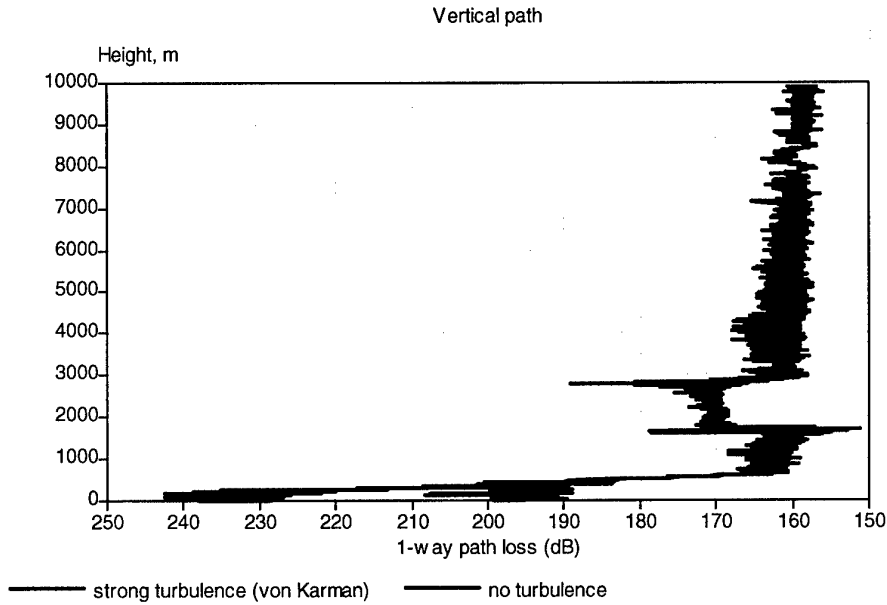
26

Figure 15: Comparison of AWACS signal at range 500 km, elevated duct environment, with and without turbulence (von Karman spectrum, $\langle n_f^2 \rangle = 10^{-6}$, $L_0 = 10$ m).
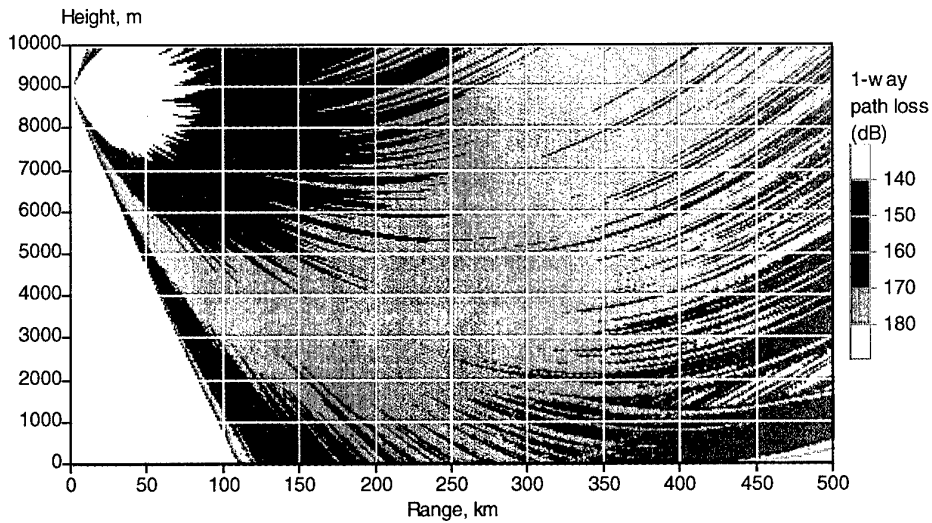

Figure 16: AWACS coverage in ducting environment, non-isotropic Gaussian spectrum, $\langle n_f^2 \rangle = 0.5 \times 10^{-6}$, $L_x = 500$ m, $L_z = 10$ m.
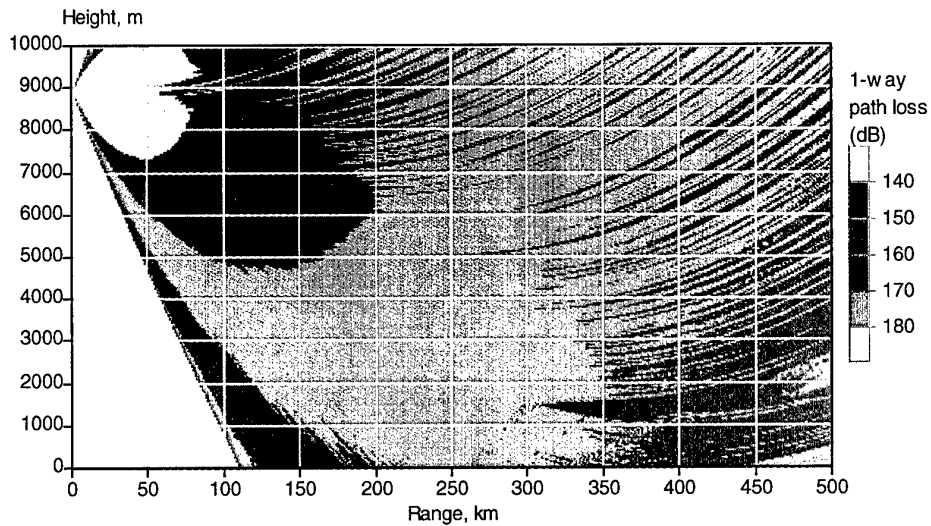
Height, m

Figure 17: AWACS coverage in ducting environment, frozen in range turbulence, Gaussian spectrum, $\langle n_f^2 \rangle = 0.5 \times 10^{-6}$, $L_z = 10$ m.
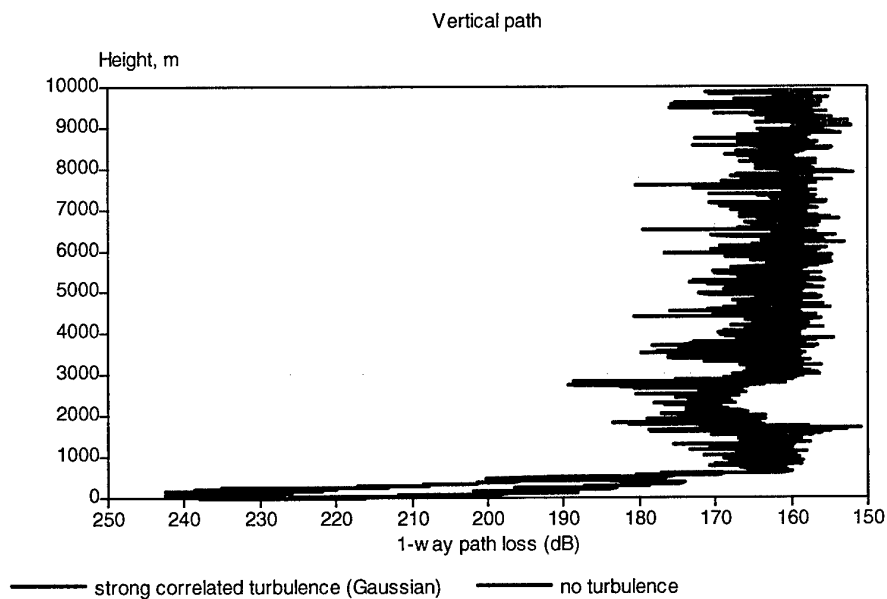
Vertical path

Height, m

——— strong correlated turbulence (Gaussian)   ——— no turbulence

Figure 18: Comparison of AWACS signal at range 500 km in elevated duct with non-isotropic Gaussian turbulence and without turbulence.
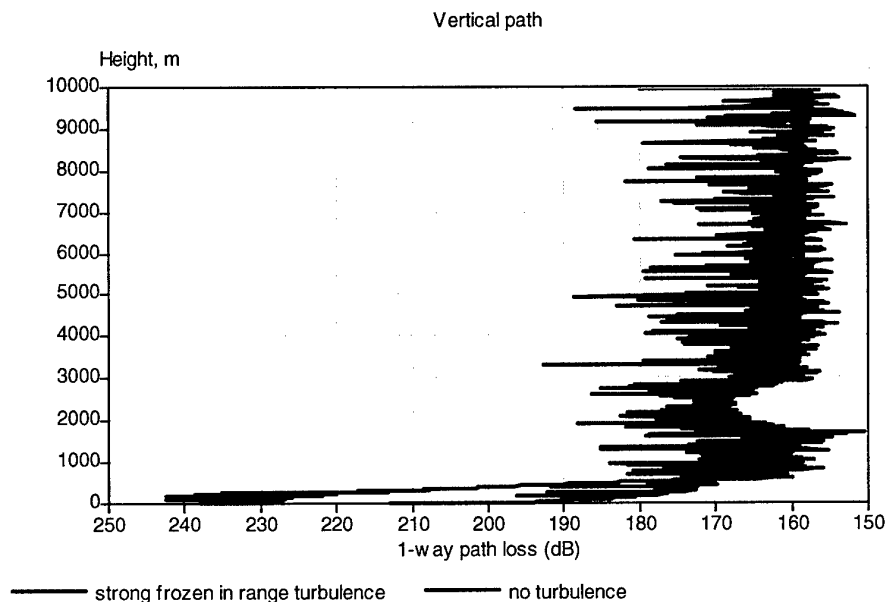
28

Figure 19: Comparison of AWACS signal at range 500 km in elevated duct with frozen in range Gaussian turbulence and without turbulence.

The PE model available at RCRU, which includes accurate treatment of the air/ground interface, has been used to compute results for generic helicopter and AWACS examples. We have used von Karman and Gaussian turbulence spectra in order to investigate the effect on non-isotropic turbulence. The case studies presented here indicate that the turbulent layers may enhance or mitigate radar holes depending on the autocorrelation function of the refractive index. These effects remain relatively small with the simulated refractivity and turbulence profiles used here, unless we assume very strong range correlation. The most striking effects are obtained for frozen-in-range turbulence, a phenomenon that was already been noticed in [6].

Several topics merit further investigation.

- The most important issue is the specification of the atmospheric environment: information on the interaction of turbulent activity with elevated duct formation is sparse, and a detailed survey on the current experimental and theoretical aspects of this problem would be most useful. In particular the question of non-isotropy, or of 3D turbulence collapse, is of crucial importance for operational consequences on AWACS missions. It is also essential to obtain high altitude measurements of the intensity of the refractive index fluctuations, since these are needed for input to numerical models.

- The examples shown here consist of individual realisations. These already give much insight into turbulence effects, but statistical results would be more significant. It

is also clear that time-dependent modelling is required in order to look at target detection and tracking when both platforms are moving.

- A detailed investigation of the accuracy of the Markov approximation for long-range simulations would be helpful. This would require some work on the generation of range-correlated phase-screens, which is a major computational problem.

References

[1] M. Abramowitz and I. A. Stegun, *Handbook of mathematical functions*, Dover Publications, Inc., New York, 1970.

[2] P. Chevret, P. Blanc-Benon and D. Juvé, "A numerical model for sound propagation through a turbulent atmosphere near the ground", *J. Acoust. Soc. Am.*, **vol. 100**, pp. 3587–3599, 1996.

[3] H. Cramér and M.R. Leadbetter, *Stationary and Related Stochastic Processes*, John Wiley and Sons, Inc., New York, 1967.

[4] R. Dashen, "Path integrals for waves in random media", *J. Math. Phys.*, **vol. 20**. pp. 894–920, 1979.

[5] G.D. Dockery and J.R. Kuttler, "An improved impedance boundary algorithm for Fourier split-step solutions of the parabolic wave equation", *IEEE Trans. Antennas Propagat.*, **vol. 44**, pp. 1592–1599, 1996.

[6] K. E. Gilbert, X. Di, S. Khanna, M. J. Otte and J. C. Wyngaard, "Electromagnetic wave propagation through simulated atmospheric refractivity fields", *IEEE Trans. Ant. Prop.*, **vol. 45**, pp. 66–72, 1997.

[7] E. E. Gossard, "Clear weather meteorological effects on propagation at frequencies above 1 GHz", *Radio Sci.*, **vol. 16**, pp. 589-608, 1981.

[8] J. A. Hermann and A. S. Kulessa, "Assessment of the role of signal fluctuations and refractive structures in microwave systems performance", DSTO Report, 1999.

[9] A. Ishimaru, *Wave propagation and scattering in random media*, New York: Academic Press, 1978.

[10] M. F. Levy and K. H. Craig, "Millimetre-wave propagation in the evaporation duct", *AGARD*, CP **454**, pp. 26.1–26.10, 1989.

[11] M. F. Levy, *Parabolic equation methods for electromagnetic wave propagation*, IEE Electromagnetic Wave Series, **45**, 2000.

[12] M. Lesieur, *Turbulence in fluids*, Kluwer Academic Publishers, Dordrecht, 1990.

[13] C. Macaskill and T.E. Ewart, "Computer simulations of two-dimensional random wave propagation". *IMA J. Appl. Math.*, **vol. 33**, pp. 1-15, 1984.

[14] E. Mandine, "Propagation électromagnétique en milieu atmosphérique aléatoire", Ph. D. Thesis, University of Toulon, 1997.

[15] A.R. Miller, R.M. Brown and E. Vegh, "New derivation for the rough-surface reflection coefficient and for the distribution of sea-wave elevations", *IEE Proc.*, **vol. 131**, part H, pp. 114–116, 1984.

[16] H.A. Panofsky and J.A. Dutton, *Atmospheric turbulence: models and methods for engineering applications*, New York: John Wiley and Sons, 1984.

[17] O.M. Phillips, "Spectral and statistical properties of the equilibrium range in wind-generated gravity waves", *J. Flui. Mech.*, **vol. 156**, pp. 505–531, 1985.

[18] W.H. Press, S.A. Teukolsky, W.T. Vetterling and B.P. Flannery, *Numerical Recipes*, Cambridge University Press, 1994.

[19] D. Rouseff, "Simulated microwave propagation through tropospheric turbulence", *IEEE Trans. Ant. Prop.*, **vol. 40**, pp. 1076–1083, 1992.

[20] J. A. Rubio, A. Belmonte and A. Comerón, "Numerical simultation of long-path spherical wave propagation in three-dimensional random media", *Opt. Eng.*, **vol. 38**, pp. 1462–1469, 1999.

[21] C. Seror, P. Saguly, C. Bailly and D. Juvé, "On the radiated noise computed by large-eddy simulations", *Physics of Fluids*, **vol. 13**, pp. 476–487, 2001.

[22] M. Spivak and B. J. Uscinski, "The split-step solution in random wave propagation", *J. Comput. Appl. Math.*, **vol. 27**, pp. 349–361, 1989.

[23] M. Spivak, "Accuracy of the moments from simulation of waves in random media", *J. Acoust. Soc. Am.*, **vol. 7**, pp. 790–793, 1990.

[24] V. I. Tatarski, *The Effects of the Turbulent Atsmophere on Wave Propagation*, U.S. Dept. of Commerce, TT-68-50464, Springfield, Virginia, 1971.

[25] J. M. Warnock and T .E. VanZandt, " A statistical model to estimate the refractivity turbulence structure constant C_n^2 in the free atmosphere", NOAA Technical Memorandum ERL AL-10, Dept. of Commerce, USA, 1985.